RSC Advances

PAPER

View Article Online
View Journal | View Issue

Cite this: *RSC Adv.*, 2019, **9**, 26364

A red-emitting $Sr_3La_{(1-x)}Eu_x(AlO)_3(BO_3)_4$ phosphor with high thermal stability and color purity for near-UV-excited wLEDs†

Cheng Yue,[a] Dachuan Zhu, *[a] Qun Yan[a] and Yong Pu[b]

A high efficiency red-emitting Eu^{3+} doped $Sr_3La(AlO)_3(BO_3)_4$ phosphor has been calcined successfully through a traditional solid-state method, and the photoluminescence and cathode-luminescence properties of samples are investigated in detail. The result of density functional theory (DFT) calculation shows that the $Sr_3La(AlO)_3(BO_3)_4$ host lattice has an indirect band gap. The broad excitation ranges from 200 nm to 500 nm, especially the strongest excitation located in the near ultraviolet (near-UV) region, suggests that the phosphor can match well with not only blue LED chips but also near-UV LED chips. Besides, the phosphor can emit bright red light peaking at 596, 618, 655 and 706 nm under either near-UV or blue light excitation and the internal quantum efficiency can reach 40%. The temperature-dependent PL properties and calculation of color purity show that the phosphor has an excellent thermal stability and outstanding color stability. Ultimately, by employing $Sr_3La(AlO)_3(BO_3)_4:Eu^{3+}$ phosphor as a red light component, a stable warm white light emission is obtained with Ra = 80, CIE = (0.3443, 0.2903) and CCT = 4680 K. These results indicate that red $Sr_3La(AlO)_3(BO_3)_4:Eu^{3+}$ phosphor may have a great potential for wLEDs with fantastic properties.

Received 3rd July 2019
Accepted 15th August 2019

DOI: 10.1039/c9ra05017e

rsc.li/rsc-advances

1. Introduction

Of late, because of their high luminous efficiency, low power consumption, long lifetime and environmental friendliness, the phosphor-converted white light-emitting diodes (wLEDs) have attracted extensive research and commercial interest.[1–4] Conventionally, wLEDs are fabricated by a blue InGaN LED chip (λ_{ex} = 450–470 nm) covered by Ce^{3+} doped yellow emitting garnet (YAG:Ce^{3+}) phosphor material. However, on account of the absence of sufficient red component, this type of wLED has a high color temperature (CCT ≈ 7750 K) and poor color rendering index (CRI ≈ 70–80) even though it has a high quantum efficiency and good thermal stability.[5–7] On the other hand, the blue light emitted by the InGaN chip can also cause damage to human eyes. Thus, the investigations of near ultraviolet white LEDs (n-UV-wLEDs) phosphors with excellent luminescence properties are necessary. Recently, a feasible method to fabricate wLED has been to combine a near ultraviolet chip and red, green and blue (RGB) phosphors. As a widely used red emission phosphor, $Y_2O_2S:Eu^{3+}$ has been used in high efficiency fluorescent lamps, cathode ray tubes, field emission displays and plasma displays, but its thermal stability and chemical stability are poor.[8] In this case, in order to improve the performances of red phosphor and wLEDs, it is an urgent task to develop novel red-emitting phosphors with excellent physical and chemical stabilities, and higher efficiencies. At present, the research of red phosphor is mainly focused on different substrates doped with Mn^{4+} or Eu^{3+}, and lots of red emission phosphors with fantastic luminescent properties have been synthesized. For example, Wang *et al.* prepared a non-rare-earth-based oxide $CaMg_2Al_{16}O_{27}:Mn^{4+}$ red phosphor, driven by a 350 mA current, the assembled w-LED device showed tunable Ra (70–85.5) and CCT (6674–3896 K).[9] In addition, Guo *et al.* made a red-emitting $Na_3Sc_2(PO_4)_3:Eu^{3+}$ phosphor with a high internal quantum efficiency of 49%.[10] Huang *et al.* also synthesized a red $Ca_3Lu(AlO)_3(BO_3)_4:Eu^{3+}$ phosphor with ultra-internal quantum efficiency of 98.5%.[11] The similar studies include $Na_{0.5}Sr_{0.25}NbO_3:Eu^{3+}$,[12] $Gd_3Zn_2Nb_3O_{14}:Eu^{3+}$,[13] $Sr[Li_2Al_2O_2N_2]:Eu^{2+}$,[14] $Na_2Gd(PO_4)(MoO_4):Eu^{3+}$ (ref. 15) and $BaGeF_6:Mn^{4+}$,[16] *etc.*, all of them have excellent luminescence properties.

As a popular red emission activator, Eu^{3+} can generate strong emission at around 620 nm corresponding to $^5D_0 \rightarrow {}^7F_2$ transition.[17–20] It is worth noting that the characteristic emission of Eu^{3+} roots in the transitions of its intra-4f electrons, and the 4f orbit lies inside the ion and is shielded from the surrounding by the filled 5s and 5p orbits. Therefore, the matrix lattice field has little effect on the optical transition within the $4f_n$ configuration, and the luminescence of Eu^{3+} ion has a good color

[a]College of Material Science and Engineering, Sichuan University, Chengdu, Sichuan, 610065, China. E-mail: zhudachuan@scu.edu.cn; Fax: +86 2885460830; Tel: +86 2885460830

[b]Research Institute for New Materials Technology, Chongqing University of Arts and Sciences, Yongchuan, Chongqing 402160, China

† Electronic supplementary information (ESI) available. See DOI: 10.1039/c9ra05017e

stability. So far, researchers have synthesized a variety of Eu^{3+} ion-doped phosphor materials with different hosts, such as tungstate, molybdate, fluoride, aluminate, oxide and phosphate.[21–26]

In this work, we have calcined the red-emitting $Sr_3La(AlO)_3(BO_3)_4$:Eu^{3+} phosphor. The relatively internal quantum efficiency (IQE) and color purity can attain to 40% and 92.40% severally with a desired doping concentration of 60 mol% Eu^{3+} ion. Under the excitation of 394 nm, the phosphor displays a strong red emission with the strongest peak at 618 nm. Finally, by employing $Sr_3La(AlO)_3(BO_3)_4$:Eu^{3+} as the red phosphor, we generate a white LED with the CCT = 4680 K and Ra = 80, which presents a substantial advance towards its commercial application. All the results indicate that the present synthesized phosphor is a suitable red-emitting applicant for n-UV-based wLEDs.

2. Experimental section

2.1. Materials and preparation

A series of $Sr_3La_{1-x}(AlO)_3(BO_3)_4$:$xEu^{3+}$ (x = 0, 10, 20, 40, 60, 80, 100 mol%) phosphor samples are calcined by the traditional solid-state reaction. The raw materials $SrCO_3$ (A. R.), La_2O_3 (A. R.), Al_2O_3 (A. R.), Eu_2O_3 (A. R.) and H_3BO_3 (A. R.) are weighed with the designed stoichiometric ratio. Of which, the excess of boric acid is 15 wt%. And then the raw materials are ground to mix adequately for 50 min. The uniform mixtures are calcined at 1050 °C for 4 h in air. Finally, the products are ground evenly into power in agate mortar for further measurements.

Based on the ratio of $Sr_3La_{0.6}Eu_{0.4}(AlO)_3(BO_3)_4$: BAM ($BaMg_2Al_{16}O_{27}$:Eu^{2+}) : $(Ca,Sr)_2SiO_4$ = 9 : 1 : 3, the three kinds of phosphors are mixed absolutely with the silicone, then the mixture is coated on the surface of a 395 nm LED chip to integrate the wLED. The wLED is drove under the current of 150 mA. The CRI, CIE chromaticity coordinates, and CCT of the wLED are measured by using the Spectrophotocolorimeter (Hongpu, Hangzhou, China).

2.2. Measurements

XRD patterns of the phosphor samples are obtained to check the phase purity by X-ray diffractometer in the 2θ range of 10–90° with a step of 0.02° min^{-1} using Cu-$K_{\alpha1}$ radiation (λ = 1.54056 Å) (XRD-6000, SHIMADZU). The band structures and corresponding density of states of $Sr_3La(AlO)_3(BO_3)_4$ host are calculated based on the density functional theory (DFT) with the Cambridge Serial Total Energy Package (CASTEP) code.[27] The exchange–correlation functional generalized gradient approximation (GGA) of Perdew–Burke–Ernzerhof (PBE) is chosen for the theoretical basis of density function with an energy cut-off of 480 V, and the k-point mesh is set as 2 × 2 × 4. The convergence criteria are set as follows: the force on the atoms is less than 0.03 eV $Å^{-1}$, the stress on the atoms is less than 0.05 GPa, the atomic displacement is less than 1×10^{-3} Å, and the energy change per atom is less than 1×10^{-5} eV. The microstructures of the calcined samples are observed by scanning electron microscopy (SEM, JSM7500, Japan). The diffuse reflectance spectra (DRS) are recorded on a UV-vis spectrophotometer (UV-3600) using the $BaSiO_4$ white power as the reference. The photoluminescence (PL) and photoluminescence excitation (PLE) spectra are measured at room temperature *via* a fluorescence spectrophotometer (F-4600, HITACHI, Japan), where the photomultiplier tube is operated at 500 V and a 150 W Xe lamp is used as the excitation source. High temperature luminescence intensity measurements are carried out by means of an aluminum plaque with cartridge heaters; the temperature is measured by thermocouples inside the plaque and controlled with a standard TAP-02 high temperature fluorescence controller (Orient KOJI instrument Co., Ltd.). Fluorescence lifetime is acquired on a Fluorolog-3 spectrofluorometer (Horiba JobinYvon) with a SpectraLED (355 nm, S-355) as the excitation source and a picosecond photon detection module (PPD-850) as the detector. The internal quantum efficiencies (IQE) are obtained on HITACHI F7000 spectrometer with excitation wavelength of 394 nm. With the help of Fluorolog Spectrofluorometer (HORIBA) equipped with an integrating sphere coated with barium sulfate, the internal quantum efficiency of the prepared samples is evaluated.

3. Results and discussion

3.1. Structure and morphology of the samples

Fig. 1 exhibits the powder X-ray reflection diffraction (PXRD) patterns for $Sr_3La_{(1-x)}Eu_x(AlO)_3(BO_3)_4$ (x = 0, 10, 20, 40, 60, 80 and 100 mol%) phosphor samples. Although the phase of $Sr_3La(AlO)_3(BO_3)_4$ cannot be indexed from ICSD files, it is found that the diffraction peaks of samples can match well with the reference diffraction lines based on $Ca_3Y(AlO)_3(BO_3)_4$ (ICSD file no. 172154). Therefore, it can be inferred that the structure of the sample is the same as that of $Ca_3Y(AlO)_3(BO_3)_4$. The Rietveld structure refinement employed the in GSAS of $Sr_3La(AlO)_3(BO_3)_4$ is shown in Fig. S1.†

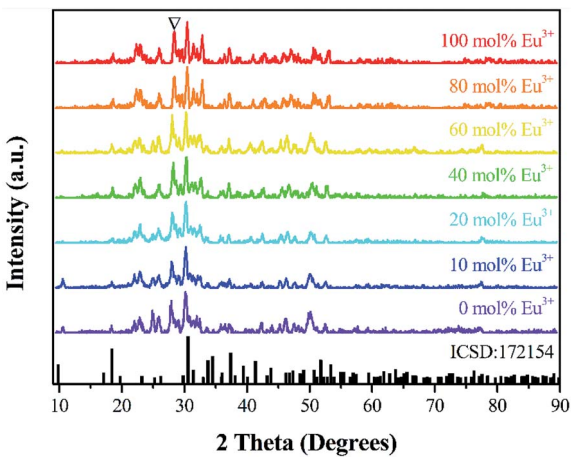

Fig. 1 PXRD patterns of $Sr_3La_{1-x}Eu_x(AlO)_3(BO_3)_4$ (x = 0, 10, 20, 40, 60, 80 and 100 mol%) phosphors calcined at 1050 °C for 4 h. The diffraction peaks of the samples are basically indexed to the pure phase of $Ca_3Y(AlO)_3(BO_3)_4$ (ICSD: 172154).

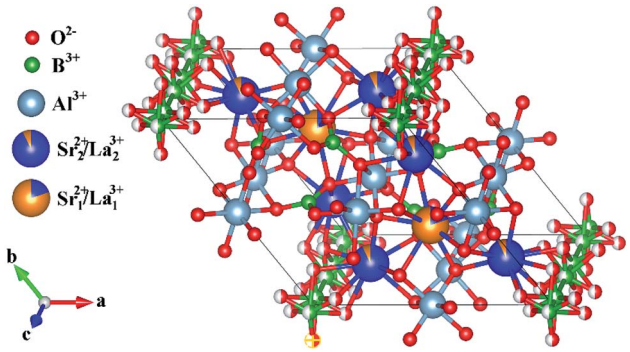

Fig. 2 The crystal structure for $Sr_3La(AlO)_3(BO_3)_4$ host showing the connectivity of Sr, La, Al, B and O, and illustration of different coordination environment.

The obtained profile factors are $R_p = 12.60\%$ and $R_{wp} = 9.82\%$. The refined lattice parameters of $Sr_3La(AlO)_3(BO_3)_4$ are $a = 10.388$ Å, $c = 5.852$ Å, $V = 546.947$ Å^3, and space group $P6_3/m$.

With the help of typical crystal structure diagram of $Sr_3La(AlO)_3(BO_3)_4$ based on the structure refinement, it is easy to comprehend the coordination environment of cations and structure character in this matrix. As shown in Fig. 2, the $Sr_3La(AlO)_3(BO_3)_4$ belong to tetragonal crystal system with the space group of $P6_3/m$, and the coordinate numbers of La_1 and La_2 are 7 and 9, respectively. For Eu^{3+}, its radius (~0.96 Å) is closer to that of La_1 (~1.06 Å), so the Eu^{3+} prefers to replace La_1 when it enters the crystal lattice of $Sr_3La(AlO)_3(BO_3)_4$.

The crystalline morphology of the $Sr_3La_{0.7}Eu_{0.3}(AlO)_3(BO_3)_4$ phosphor is checked by scanning electron microscopy (shown in Fig. 3a), and the accordingly energy dispersive X-ray analysis (EDX) is employed to identify the content of different elements as exhibited in Fig. 3b. In Fig. 3c, it is clearly seen from the images that the samples are composed of agminated particles with sizes ranging from 5 to 15 μm and the average size is about ~9 μm.

3.2. Energy gap, electronic structure and density of state (DOS)

To get insight into the electronic properties of $Sr_3La(AlO)_3(BO_3)_4$ host matrix, the band structure and density of states (DOS) are computed and plotted in Fig. 4 after optimizing the $Sr_3La(AlO)_3(BO_3)_4$ structure. In Fig. 4a, the band gap between conduction bands minimum and valence bands maximum is about 4.57 eV, and they are located at G and K point in Brillouin zone severally, indicating that this host presents an indirect band gap. Therefore, the structure of $Sr_3La(AlO)_3(BO_3)_4$ is influential to luminescence since the transition probability of the indirect band gap is lower than that of the direct band gap due to the phonons involved in the transition process. In addition, the valence band of $Sr_3La(AlO)_3(BO_3)_4$ is remarkably flat, which reveals the very low mobility of the holes. By contrast, the dispersion of electronic states forming the conduction band is pronounced. With the help of density of states (DOS) and atomic partial density of states (PDOS) in Fig. 4b, we can acquire more information. The valence bands are dominated by the 2s orbit of O, 5p orbit of La and 4p of Sr, while the conduction bands comprise the 2p orbit of O, 2s and 2p orbits of B, 6s of La and 5s of Sr.

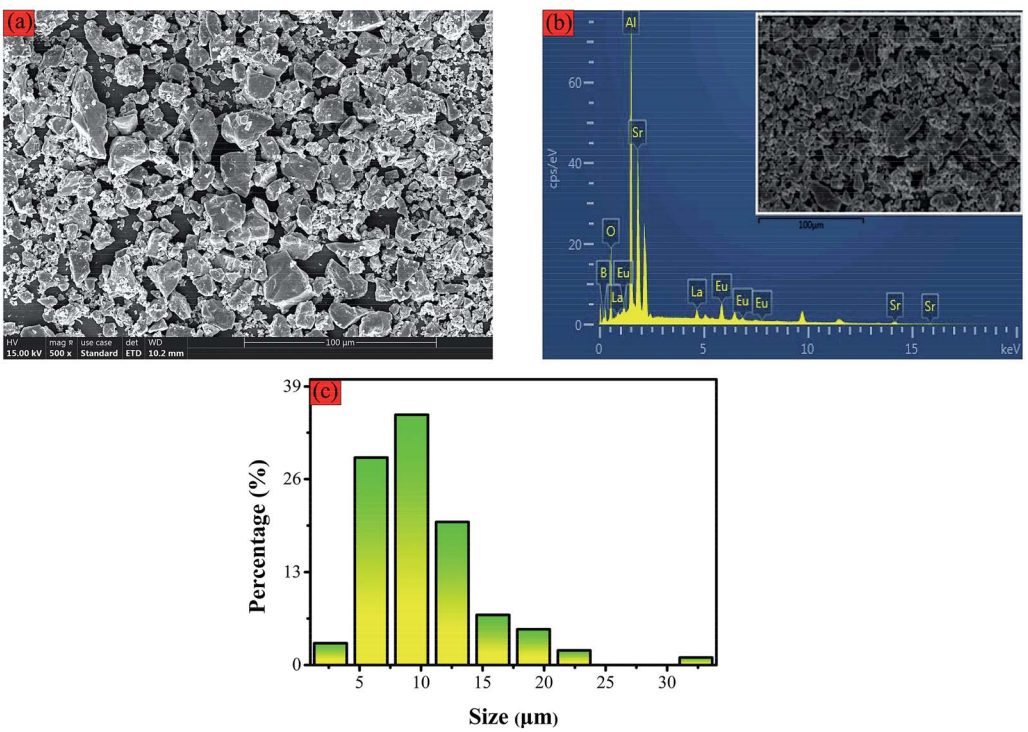

Fig. 3 (a) SEM image of the as-prepared $Sr_3La_{0.7}Eu_{0.3}(AlO)_3(BO_3)_4$ phosphor with magnification of 500; (b) EDX; (c) distribution of size.

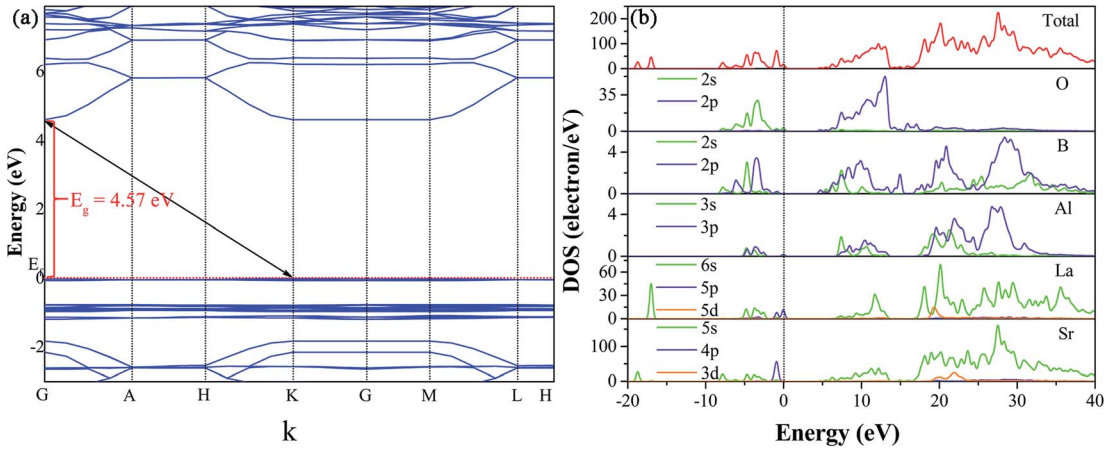

Fig. 4 Band structure and density of states for $Sr_3La(AlO)_3(BO_3)_4$ crystal.

In order to analyze the absorption spectroscopy, the diffuse reflection spectrum (DRS) of $Sr_3La(AlO)_3(BO_3)_4$ host and $Sr_3La_{0.4}Eu_{0.6}(AlO)_3(BO_3)_4$ phosphor are measured, as shown in Fig. 5a. Obviously, compared with the $Sr_3La(AlO)_3(BO_3)_4$ host, the diffuse reflectance spectrum of $Sr_3La_{0.4}Eu_{0.6}(AlO)_3(BO_3)_4$ shows an intense broad absorption band in the 200–300 nm range deriving from the $Eu^{3+} \rightarrow O^{2-}$ charge transfer band (CTB). In addition, a battery of relatively sharp peaks at 362 nm, 380 nm, 395 nm, 416 nm, 465 nm, 532 nm and 591 nm can be ascribed to 4f–4f transitions of Eu^{3+} ions ($^7F_0 \rightarrow {}^5D_4$, $^7F_0 \rightarrow {}^5L_7$, $^7F_0 \rightarrow {}^5L_6$, $^7F_0 \rightarrow {}^5D_3$, $^7F_0 \rightarrow {}^5D_2$, $^7F_1 \rightarrow {}^5D_1$ and $^7F_1 \rightarrow {}^5D_0$, respectively). To further discuss the energy levels, the energy gap can be calculated according to the following function:[28]

$$[F(R_\infty)h\nu]^n = c(h\nu - E_g) \quad (1)$$

where $h\nu$ is the photon energy, c is a proportional constant, E_g is the value of the band gap, $n = 2$ for a direct transition or 1/2 for an indirect transition. The $F(R_\infty)$ can be described by the Kubelka–Munk function:[29]

$$F(R_\infty) = \frac{(1-R)^2}{2R} = K/S \quad (2)$$

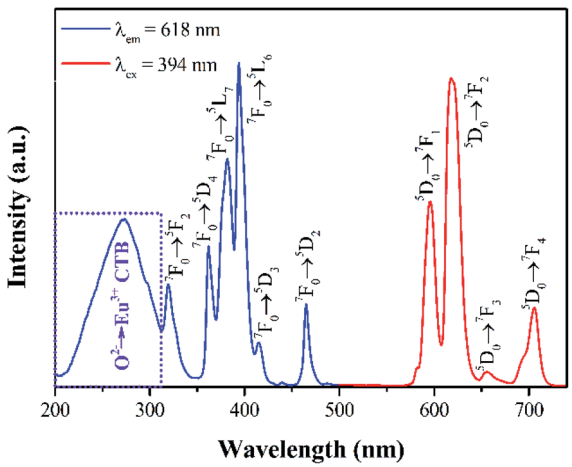

Fig. 6 The PL (λ_{ex} = 394 nm) and PLE (λ_{em} = 618 nm) spectra of $Sr_3La(AlO)_3(BO_3)_4$:Eu^{3+} phosphor.

Here, R, K and S are the reflection, the absorption and the scattering coefficient, respectively. From the linear extrapolation of $[F(R_\infty)h\nu]^{1/2} = 0$, the E_g value of $Sr_3La(AlO)_3(BO_3)_4$ host

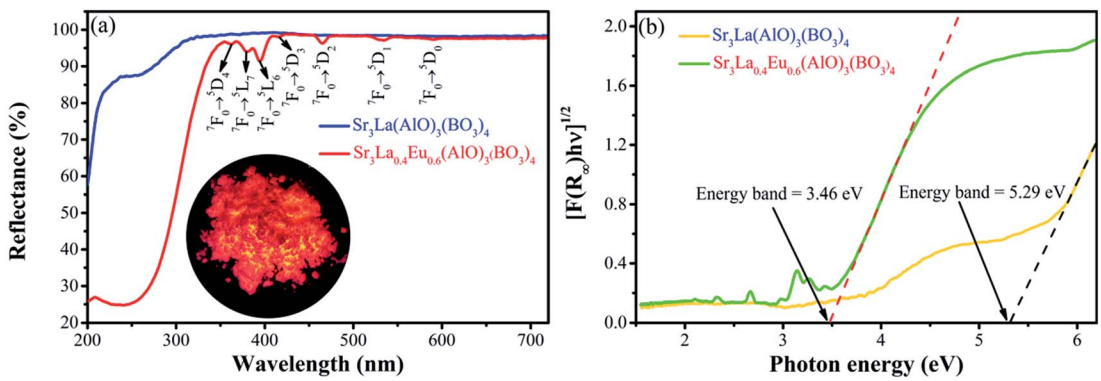

Fig. 5 (a) DRS of $Sr_3La(AlO)_3(BO_3)_4$ host and $Sr_3La_{0.4}Eu_{0.6}(AlO)_3(BO_3)_4$; (b) absorption spectrum of $Sr_3La(AlO)_3(BO_3)_4$ host and $Sr_3La_{0.4}Eu_{0.6}(AlO)_3(BO_3)_4$ as calculated by the Kubelka–Munk formula.

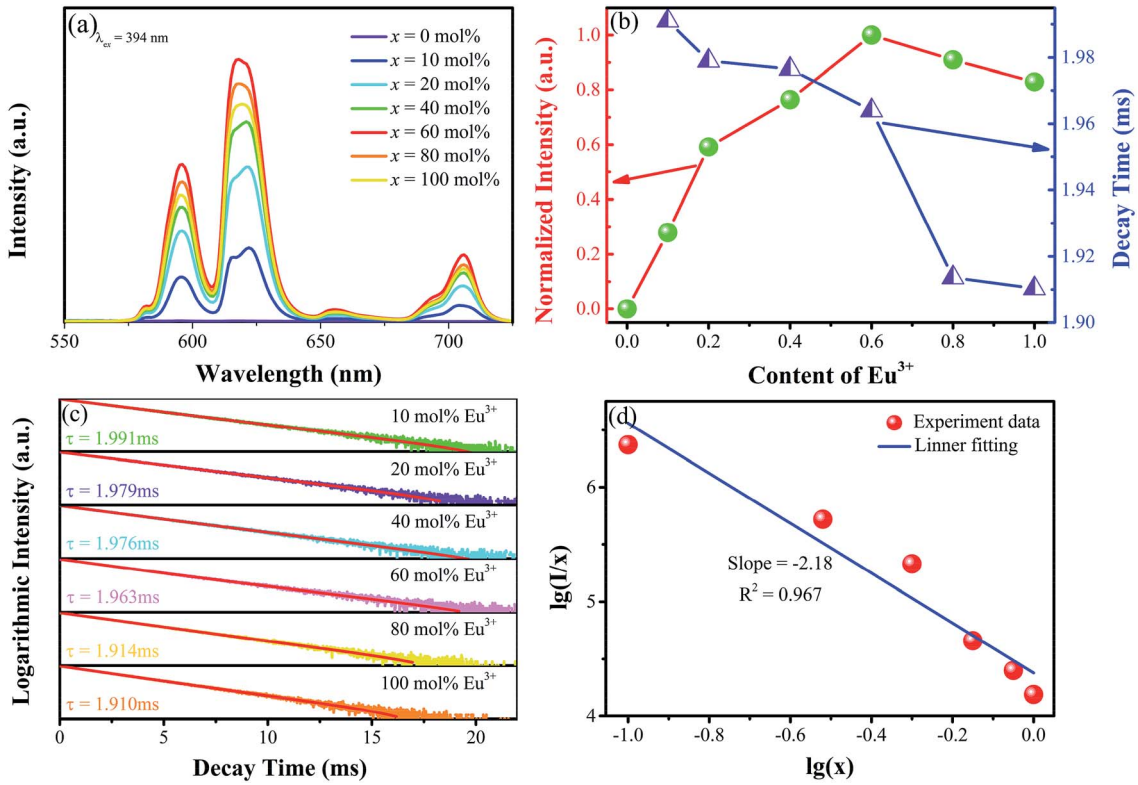

Fig. 7 Room-temperature (a) emission and (b) fluorescence decay curves (excited at 394 nm and monitored at 618 nm), (c) normalized integrated intensity and lifetimes of Eu^{3+} in $Sr_3La_{1-x}Eu_x(AlO)_3(BO_3)_4$ with various Eu^{3+} concentrations, and (d) lg(I/x) *vs.* lg(x).

Table 1 The fitting results and average lifetimes of fluorescence decay curves of $Sr_3La_{1-x}Eu_x(AlO)_3(BO_3)_4$

Concentration of Eu^{3+} (mol%)	τ_1 (ms)	τ_2 (ms)	A_1	A_2	τ^* (ms)
10	2.63	1.93	790	8872	1.991
20	2.96	3.79	9644	117	1.979
40	1.68	2.12	3100	6550	1.976
60	1.65	2.27	4808	4882	1.964
80	1.88	2.64	9276	488	1.914
100	2.58	1.86	707	9053	1.910

and $Sr_3La_{0.4}Eu_{0.6}(AlO)_3(BO_3)_4$ are estimated to be about 5.29 and 3.46 eV (see Fig. 5b) severally, indicating that the energy gap is reduced after doping the Eu^{3+}. In general, the real band gap is higher than theoretical value sometimes since DFT-calculated band gaps are always underestimated (The unmodified exchange correlation function is applied in DFT calculation).[30]

3.3. Photoluminescence properties

The room-temperature photoluminescence excitation spectra (λ_{em} = 618 nm) and emission (λ_{ex} = 356 nm, 365 nm, 377 nm, 404 nm, 449 nm, 488 nm) of $Sr_3La_{0.4}Eu_{0.6}(AlO)_3(BO_3)_4$ calcined at 1050 °C are shown in Fig. 6. The PLE spectrum of $Sr_3La_{0.4}Eu_{0.6}(AlO)_3(BO_3)_4$ phosphor consists of a broad band in the 250–300 nm region peaking at about 272 nm and several intense sharp lines in the 300–470 nm region, indicating that these

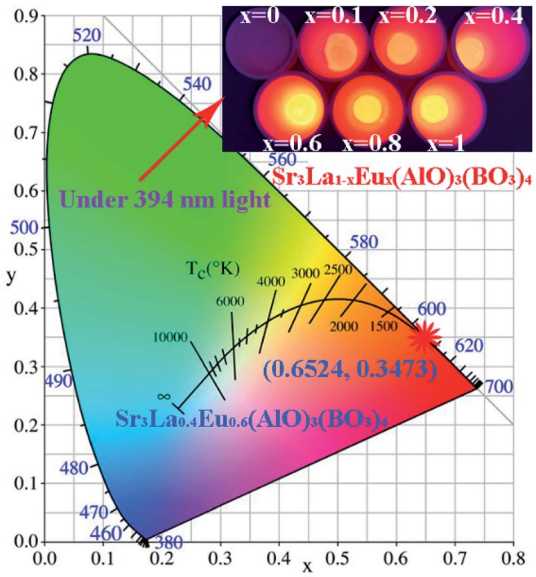

Fig. 8 CIE (x, y) coordinate diagram showing chromaticity points of Eu^{3+} luminescence in $Sr_3La_{0.4}Eu_{0.6}(AlO)_3(BO_3)_4$; insets are the corresponding luminescent photos under 394 nm UV lamp illumination.

phosphors can be effectively excited by UV LED chip (350–400 nm). The PLE spectra exhibit several peaks at 319 nm, 362 nm, 382 nm, 394 nm, 414 nm and 465 nm, which can be attributed to the $^7F_0 \rightarrow {}^5F_2$, $^7F_0 \rightarrow {}^5D_4$, $^7F_0 \rightarrow {}^5L_7$, $^7F_0 \rightarrow {}^5L_6$, $^7F_0 \rightarrow {}^5D_3$,

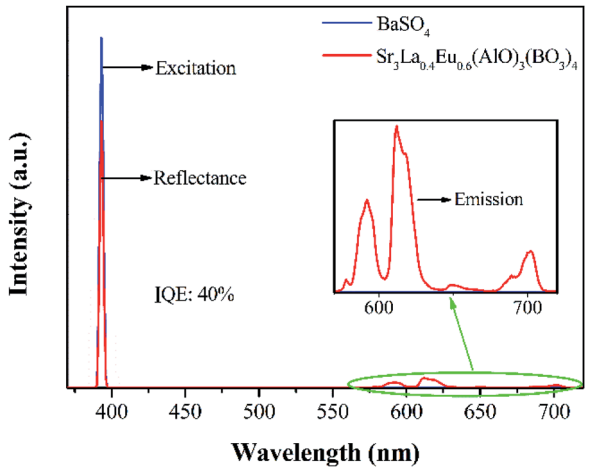

Fig. 9 Room-temperature excitation of $BaSiO_4$ and reflection and emission of $Sr_3La_{0.4}Eu_{0.6}(AlO)_3(BO_3)_4Eu^{3+}$.

Table 2 IQE of $Sr_3La_{1-x}Eu_x(AlO)_3(BO_3)_4$ (λ_{ex} = 394 nm)

Sample no.	Concentration of Eu^{3+} (mol%)	IQE (%)
1	10	27
2	20	33
3	40	38
4	60	40
5	80	37
6	100	33

$^7F_0 \rightarrow {}^5D_2$ transitions of Eu^{3+} ions separately. This result corresponds well to that of DRS. The broad band is attributed to the charge transfer band (CTB) transition from the fully filled 2p orbits of O^{2-} ions to the partially filled 4f orbits of Eu^{3+}.[8,17,18,31] Besides, the PL spectrum shows a red emission with the peaks at 596 nm, 618 nm, 655 nm and 706 nm, which result from the transition of $^5D_0 \rightarrow {}^7F_1$, $^5D_0 \rightarrow {}^7F_2$, $^5D_0 \rightarrow {}^7F_3$, $^5D_0 \rightarrow {}^7F_4$.

To obtain the best doping content of Eu^{3+}, the emission spectra of $Sr_3La_{(1-x)}Eu_x(AlO)_3(BO_3)_4$ have been investigated. As shown in Fig. 7a, under the excitation of 394 nm, the emission intensity keeps increasing until the value of x = 60 mol%, beyond which the concentration quenching occurs and the emission intensity begins to decrease. Therefore, the optimal doped concentration is about 60 mol%, it is also displayed by the corresponding tendency chart in Fig. 7b. In general, when the concentration of activator ions increases, the distance between the activators decreases, leading to the enhancement in energy transfer between the activators. If the ions concentration continues to increase, it will cause fluorescence quenching.

The photoluminescence decay curves of the samples also reveal the dependence of photoluminescence properties on the activator concentration and can provide important information of the concentration quenching in the energy transfer process. The fluorescence decay lifetime measurements for Eu^{3+} emission (λ_{ex} = 394 nm, λ_{em} = 618 nm) with Eu^{3+} concentration increasing are shown in Fig. 7c and the corresponding tendency is shown in Fig. 7b. All the fluorescence intensities show the trend of fast decay first and then slow decrease. And the Eu^{3+} decay curves of $Sr_3La_{1-x}Eu_x(AlO)_3(BO_3)_4$ (x = 10, 20, 40, 60, 80, 100 mol%) samples can be well fitted with a second-order exponential decay equation (defects in the samples might act as the channels of non-radiative relaxation) as:[32,33]

$$I(t) = I_0 + A_1 \exp\left(-\frac{t}{\tau_1}\right) + A_2 \exp\left(-\frac{t}{\tau_1}\right) \quad (3)$$

$$\tau^* = (A_1\tau_1^2 + A_2\tau_2^2)/(A_1\tau_1 + A_2\tau_2) \quad (4)$$

where $I(t)$ is the fluorescence intensity at time t and I_0 is the background luminescence intensity, A_1 and A_2 are constants while τ_1 and τ_2 are the decay times for the double-exponential components, respectively. The fitting parameters are listed in Table 1, showing that the lifetime of Eu^{3+} in $Sr_3La_{1-x}Eu_x(AlO)_3(BO_3)_4$ is in the range of microsecond, which is reasonable for the $^5D_0 \rightarrow {}^7F_2$ transitions of Eu^{3+}. With increasing Eu^{3+} concentration, the lifetime becomes shorter gradually from 1.991 ms to 1.910 ms, it can be attributed to the increased non-radiative energy transfer. At the same time, it is worth noting that the decrease in fluorescence decay lifetime is very small (0.081 ms), this is an interesting phenomenon.

In order to further investigate the quenching mechanism, it is necessary to calculate the critical transfer distance (R_c). According to Blasse's theory, the critical distance R_c can be calculated approximately by this equation:[34]

$$R_c \approx 2\left(\frac{3V}{4\pi x_c N}\right)^{1/3} \quad (5)$$

where the V is the volume of the unit cell, x_c is the critical concentration from Fig. 7a, and N is the number of available sites for the dopant (Eu^{3+}) in the unit cell. In this case, V = 531.92 Å^3,[35] x_c = 0.6, N = 2, so the critical distance for Eu^{3+} in $Sr_3La(AlO)_3(BO_3)_4$:Eu^{3+} is calculated to be ~9.16 Å. It can be inferred that the concentration quenching mainly takes place *via* electric multipolar interaction between Eu^{3+} ions because the exchange interaction is dominant only for short critical transfer distance (R_c < 5 Å) based on the Dexter's theory.[36] Hence concentration quenching process must be controlled by electric multipole interactions. Generally, there are three multipole interactions, namely, dipole–dipole, dipole–quadrupole and quadrupole–quadrupole interactions. In order to further investigate the concentration quenching mechanism in the phosphor, the following equation is used:[37]

$$\frac{I}{x} = \kappa\left[1 + \beta(x)^{\frac{\theta}{3}}\right]^{-1} \quad (6)$$

where I represents the emission intensity of Eu^{3+} with different content, x is the concentration of Eu^{3+}, β and κ are the constants at some condition, and θ equals to 6, 8, 10 for dipole–dipole, dipole–quadrupole, quadrupole–quadrupole, respectively.

The relationship between lg(I/x) and lg(x) has been plotted as shown in Fig. 7d. The slope of line is about −2.18, and the calculated $\theta \approx 6$, meaning that the concentration quenching

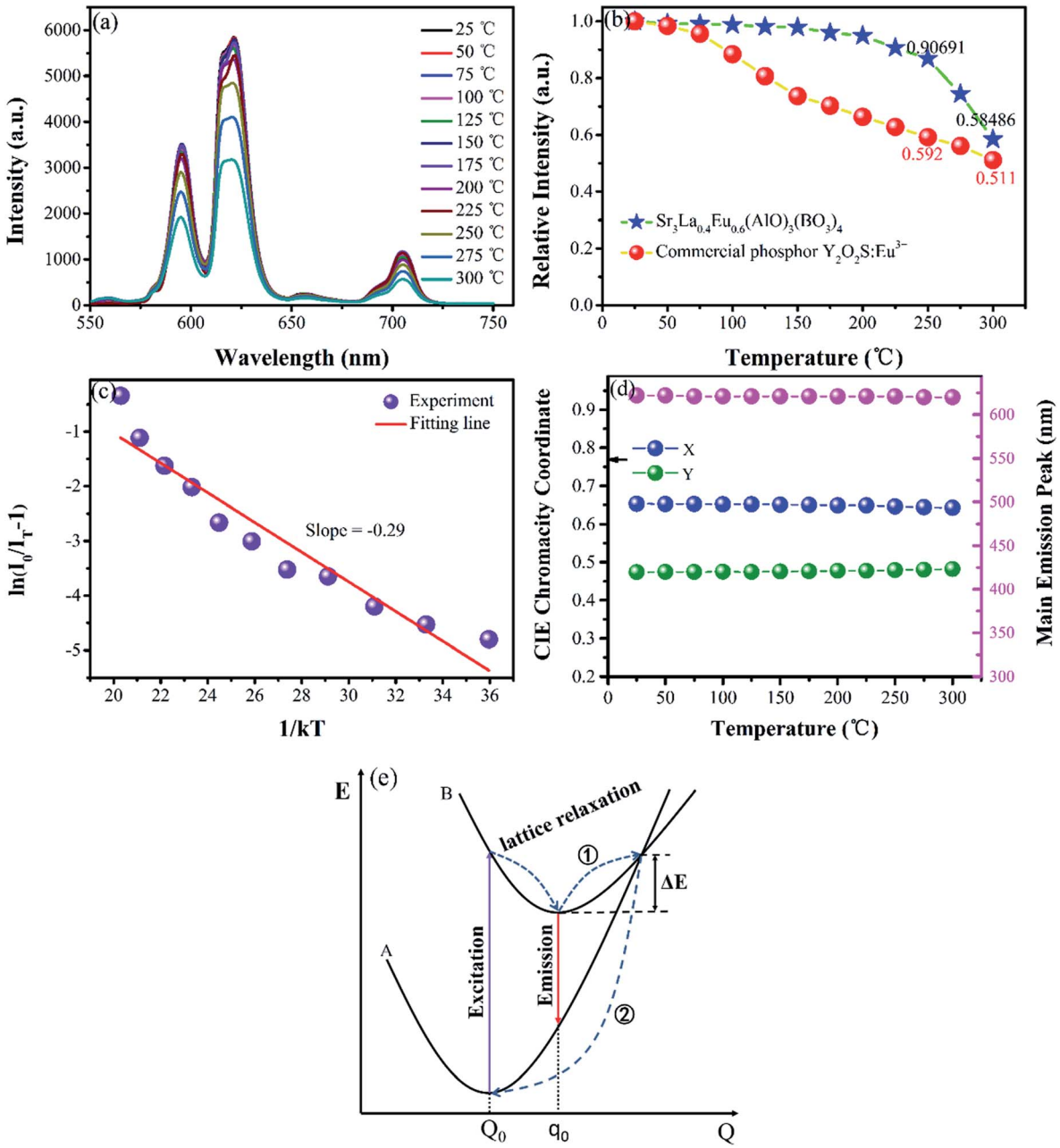

Fig. 10 (a) Temperature-dependent emission spectra of $Sr_3La_{0.4}Eu_{0.6}(AlO)_3(BO_3)_4$ in the range ~25–300 °C, (b) comparisons of corresponding integrated emission intensity between $Sr_3La_{0.4}Eu_{0.6}(AlO)_3(BO_3)_4$ and $Y_2O_2S:Eu^{3+}$ as a function of temperature, (c) the linear fitting curve of $\ln(I_0/I_T - 1)$ *versus* $1/kT$ for the $Sr_3La_{0.4}Eu_{0.6}(AlO)_3(BO_3)_4$ phosphor, (d) the color stability with different temperature and (e) configurational coordinate diagram of the ground state and excited state of Eu^{3+}.

mechanism between the closer Eu^{3+} ions in the $Sr_3La_{1-x}Eu_x(AlO)_3(BO_3)_4$ is dominated by dipole–dipole interaction.

Furthermore, the luminescence color of $Sr_3La_{1-x}Eu_x(AlO)_3(BO_3)_4$ has been characterized using CIE 1931 chromaticity diagram. The CIE coordinate value of the $Sr_3La_{0.4}Eu_{0.6}(AlO)_3(BO_3)_4$ phosphor is calculated to be (0.6524, 0.3473), situated in the red region and at the extreme corner of the CIE diagram as shown in Fig. 8.

To get a deep insight into the chromatic behaviors of the obtained red emission, its color purity is calculated with the help of the following formula:[38,39]

$$\text{Color purity} = \frac{\sqrt{(x - x_i)^2 - (y - y_i)^2}}{\sqrt{(x_d - x_i)^2 - (y_d - y_i)^2}} \times 100\% \quad (7)$$

In the expression, the (x, y), (x_i, y_i) and (x_d, y_d) refer to the CIE coordinates of the synthesized compounds, white illumination and dominant wavelength, respectively. In this present work, $(x, y) = (0.6524, 0.3466)$, $(x_i, y_i) = (0.310, 0.316)$ and $(x_d, y_d) = (0.679, 0.317)$. As a result, the color purity of the achieved red emission

is demonstrated to be about 92.40%, which is superior to some previous developed red-emitting phosphors, such as $Na_3Sc_2(PO_4)_3:Eu^{3+}$ (87%)[10] and $Na_2Gd(PO_4)(MoO_4):Eu^{3+}$ (92%).[15]

3.4. Quantum efficiency

The internal quantum efficiency (IQE) of $Sr_3La_{1-x}Eu_x(AlO)_3(BO_3)_4$ phosphors are calculated by using the following equations:[40]

$$\mathrm{IQE} = \frac{\int L_S}{\int E_R} \quad (8)$$

In which L_S stands for the emission spectrum of the phosphor, and E_R represents the spectrum of excitation light without phosphor in integrating sphere. The IQE of $Sr_3La_{0.4}Eu_{0.6}(AlO)_3(BO_3)_4$ is calculated to be about 40%, as shown in Fig. 9. And the IQEs of $Sr_3La_{1-x}Eu_x(AlO)_3(BO_3)_4$ are displayed in Table 2.

3.5. Thermal stability

Thermal stability is another important performance factor for phosphors because LED chips will produce a large amount of heat in operation. To further verify the thermal stability characteristic of $Sr_3La(AlO)_3(BO_3)_4:Eu^{3+}$, thermal quenching of the typical $Sr_3La_{0.4}Eu_{0.6}(AlO)_3(BO_3)_4$ sample is investigated in detail. The temperature-dependent emission spectra and emission intensity are also given in Fig. 10a. With temperature increasing, the peak positions and band shape of this phosphor do not vary, whereas the emission intensity changes obviously. In order to better compare the thermal stability, Fig. 10b exhibits the emission intensities of $Sr_3La_{0.4}Eu_{0.6}(AlO)_3(BO_3)_4$ and commercial $Y_2O_3S:Eu^{3+}$ phosphors depend on temperature. Apparently, as the temperature increases, the emission intensities of these two kinds of phosphors have a similar trend to decrease. Specifically, at 225 °C, the emission intensity of $Sr_3La_{0.4}Eu_{0.6}(AlO)_3(BO_3)_4$ can still remain at ~91% of the initial value (at ~25 °C), while that of the $Y_2O_3S:Eu^{3+}$ reduces to ~59%. When the temperature further rises to 300 °C, the emission intensity of $Sr_3La_{0.4}Eu_{0.6}(AlO)_3(BO_3)_4$ decreases to 59% of the initial value, while that of the $Y_2O_3S:Eu^{3+}$ decreases to 51%. The fact suggests that the $Sr_3La(AlO)_3(BO_3)_4:Eu^{3+}$ phosphor has a better thermal stability. Usually, the activation energy can be calculated using the Arrhenius equation:[41]

$$I_T = \frac{I_0}{1 + c\exp\left(-\frac{\Delta E}{kT}\right)} \quad (9)$$

where I_0 and I_T represent the emission intensity at room temperature and testing temperature, respectively, c is a constant, ΔE is the activation energy for thermal quenching, and k is Boltzmann's constant (8.617105×10^{-5} eV K^{-1}). The dependence of $\ln[(I_0/I_T) - 1)]$ on $1/kT$ is shown in Fig. 10c. From the straight slope, ΔE is calculated as 0.29 eV. The high activation energy causes a good thermal stability of phosphor. As shown in Fig. 10d, it is noteworthy that the peak position and CIE color coordinates of the $Sr_3La(AlO)_3(BO_3)_4:Eu^{3+}$ phosphor keep almost constant during the continuous heating from 25 °C to 300 °C, which implies that the $Sr_3La(AlO)_3(BO_3)_4:Eu^{3+}$ phosphor has an excellent color stability. The above facts strongly suggest that red $Sr_3La(AlO)_3(BO_3)_4:Eu^{3+}$ phosphor has a great potential to be applied in w-LEDs.

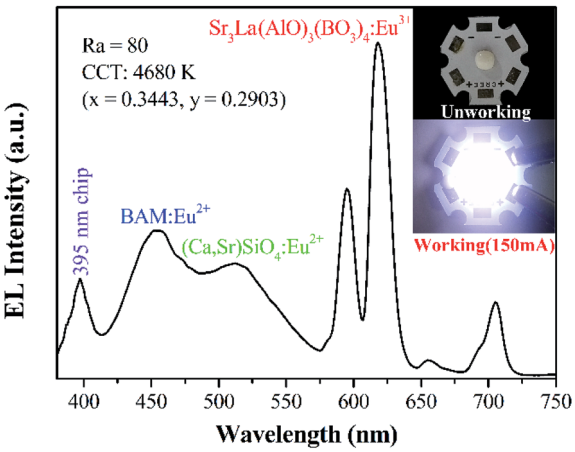

Fig. 11 EL spectrum of the fabricated white LED lamp by 150 mA current. The insets are the photos of LED when not working and working.

The thermal quenching can be explained by configurational coordinate diagram. In Fig. 10e, the symbols of A and B represent the ground state and excited state of Eu^{3+} separately. As the temperature increases, the lattice vibration of the matrix increases, and the electrons in the excited state can be thermally activated to reach the intersection of the ground state and the excited state coordinate curve (process ①), causing the excited state electrons to transit to the ground state non-radioactively and pass through the lattice relaxation to reach the equilibrium state of the ground state (process ②). As a result, the two processes are enhanced as the temperature continues to rise, and the luminescence intensity becomes weaker at higher temperatures.

Encapsulation experiment is actualized to evaluate the potential application possibility for $Sr_3La(AlO)_3(BO_3)_4:Eu^{3+}$. By employing the $Sr_3La(AlO)_3(BO_3)_4:Eu^{3+}$ phosphor as a red component, the white light can be generated with Ra = 80, CCT = 4680 K and CIE of (0.3443, 0.2903) under the driven current of 150 mA. The corresponding electroluminescence (EL) spectrum of the fabricated white LED is shown in Fig. 11. The obtained warm white light has a high color index, indicating that the $Sr_3La(AlO)_3(BO_3)_4:Eu^{3+}$ phosphor has a great potential to be applied in w-LED.

4. Conclusion

In summary, a series of highly efficient Eu^{3+}-activated $Sr_3La(AlO)_3(BO_3)_4$ phosphors are successfully prepared by the solid-state reaction method. The resultant phosphor could be efficiently excited by the commercial NUV chip and emitted brightly visible red emission with a high color purity of approximately 92.40%. The optimal doping concentration of Eu^{3+} ions in the $Sr_3La\ (AlO)_3(BO_3)_4$ host material is determined to be as high as 60 mol% and the dipole–dipole interaction

contributes to the concentration quenching. Furthermore, the internal quantum efficiency of the $Sr_3La_{0.4}Eu_{0.6}(AlO)_3(BO_3)_4$ phosphor is found to be 40%. The temperature-dependent PL emission spectra revealed that the studied phosphor possessed excellent thermal stability with an activation energy of 0.29 eV. By employing $Sr_3La(AlO)_3(BO_3)_4$:Eu^{3+} as a red light component, a stable wLED with proper CCT (4680 K) and CRI (Ra = 80) values is obtained. The above results indicate that red phosphor $Sr_3La(AlO)_3(BO_3)_4$:Eu^{3+} may be a promising candidate for fabricating near ultraviolet converted white-light LEDs.

Conflicts of interest

There are no conflicts of interest to declare.

Acknowledgements

This work was supported by the Science and Technology Research Program of Chongqing Municipal Education Commission (Grant No. KJQN201801332) and The Fundamental Research Funds for Central Universities.

References

1 L. J. Yin, Y. L. Liang, S. H. Zhang, M. Wang, L. Li, W. J. Xie, H. Zhong, X. Jian, X. Xu, X. Wang and L. J. Deng, *Chem. Commun.*, 2018, **54**, 3480–3483.
2 H. Daicho, Y. Shinomiya, K. Enomoto, A. Nakano, H. Sawa, S. Matsuishi and H. Hosono, *Chem. Commun.*, 2018, **54**, 884–887.
3 L. Wang, R. J. Xie, Y. Li, X. Wang, C. G. Ma, D. Luo, T. Takeda, Y. T. Tsai, R. S. Liu and N. Hirosaki, *Light: Sci. Appl.*, 2016, **5**, e16155.
4 F. Yang, Y. Liu, X. Tian, G. Dong and Q. Yu, *J. Solid State Chem.*, 2015, **225**, 19–23.
5 C. Feldmann, T. Jüstel, C. R. Ronda and P. J. Schmidt, *Adv. Funct. Mater.*, 2003, **13**, 511–516.
6 R.-J. Xie, N. Hirosaki, T. Suehiro, F.-F. Xu and M. Mitomo, *Chem. Mater.*, 2006, **28**, 5578–5583.
7 C. Zhao, D.-c. Zhu, W. Gao, M.-j. Tu, L.-l. Luo, T. Han and X.-l. Jing, *Chem. Eng. J.*, 2014, **254**, 486–490.
8 J. Qiao, L. Wang, Y. Liu, P. Huang, Q. Shi, Y. Tian and C. e. Cui, *J. Alloys Compd.*, 2016, **686**, 601–607.
9 B. Wang, H. Lin, J. Xu, H. Chen and Y. Wang, *ACS Appl. Mater. Interfaces*, 2014, **6**, 22905–22913.
10 H. Guo, X. Huang and Y. Zeng, *J. Alloys Compd.*, 2018, **741**, 300–306.
11 X. Huang, S. Wang, B. Li, Q. Sun and H. Guo, *Opt. Lett.*, 2018, **43**, 1307–1310.
12 Y. Shi, B. Quan, Q. Ning, S. Cao, J. Shi and C. Dong, *Mater. Res. Bull.*, 2018, **101**, 363–370.
13 T. S. Sreena, P. P. Rao, A. K. V. Raj and T. R. A. Thara, *J. Alloys Compd.*, 2018, **751**, 148–158.
14 X. Huang, *Sci. Bull.*, 2019, **64**, 879–880.
15 X. Huang, H. Guo and B. Li, *J. Alloys Compd.*, 2017, **720**, 29–38.
16 Q. Zhou, Y. Zhou, Y. Liu, L. Luo, Z. Wang, J. Peng, J. Yan and M. Wu, *J. Mater. Chem. C*, 2015, **3**, 3055–3059.
17 J. Zhao, C. Guo, T. Li, X. Su, N. Zhang and J. Chen, *Dyes Pigm.*, 2016, **132**, 159–166.
18 P. Du and J. S. Yu, *J. Lumin.*, 2016, **179**, 451–456.
19 P. Du, X. Huang and J. S. Yu, *Chem. Eng. J.*, 2018, **337**, 91–100.
20 S. Wang, Y. Xu, T. Chen, W. Jiang, J. Liu, X. Zhang, W. Jiang and L. Wang, *J. Alloys Compd.*, 2019, **789**, 381–391.
21 R. Cao, C. Liao, F. Xiao, G. Zheng, W. Hu, Y. Guo and Y. Ye, *Dyes Pigm.*, 2018, **149**, 574–580.
22 N. D. Quoc Anh, H.-Y. Lee, T. Thanh Phuong, N. H. Khanh Nhan, T. H. Quang Minh and T. Huu Ly, *J. Chin. Inst. Eng.*, 2017, **40**, 228–234.
23 N. Dhananjaya, C. Shivakumara, R. Saraf and H. Nagabhushana, *Mater. Res. Bull.*, 2016, **75**, 100–109.
24 F. M. Emen, R. Altinkaya, V. E. Kafadar, G. Avsar, T. Yeşilkaynak and N. Kulcu, *J. Alloys Compd.*, 2016, **681**, 260–267.
25 H. Pan, X. Lin, J. Zhang, L. Guan, H. Su and F. Teng, *Mater. Lett.*, 2015, **155**, 106–108.
26 X. Huang, B. Li, H. Guo and D. Chen, *Dyes Pigm.*, 2017, **143**, 86–94.
27 S. J. Clark, M. D. Segall, C. J. Pickard, P. J. Hasnip, M. I. J. Probert, K. Refson and M. C. Payne, *Z. Kristallogr. - Cryst. Mater.*, 2005, **220**, 567–570.
28 B. Wang, Z. Wang, Y. Liu, T. Yang, Z. Huang and M. Fang, *J. Alloys Compd.*, 2019, **776**, 554–559.
29 D. Deng, H. Yu, Y. Li, Y. Hua, G. Jia, S. Zhao, H. Wang, L. Huang, Y. Li, C. Li and S. Xu, *J. Mater. Chem. C*, 2013, **1**, 3194–3199.
30 X. Wang, Z. Zhao, Q. Wu, Y. Li and Y. Wang, *Inorg. Chem.*, 2016, **55**, 11072–11077.
31 X. Zhang and D. Miao, *Knowl. Based Syst.*, 2016, **91**, 219–240.
32 J. Wang, H. Zhang, B. Lei, Z. Xia, H. Dong, Y. Liu, M. Zheng and Y. Xiao, *J. Mater. Chem. C*, 2015, **3**, 4445–4451.
33 Z. Chen, Y. Pan, L. Xi, R. Pang, S. Huang and G. Liu, *Inorg. Chem.*, 2016, **55**, 11249–11257.
34 G. Blasse, *Phys. Lett. A*, 1968, **28**, 444–445.
35 Y. Yu, Q. S. Wu and R. K. Li, *J. Solid State Chem.*, 2006, **179**, 429–432.
36 D. L. Dexter, *J. Chem. Phys.*, 1953, **21**, 836–850.
37 L. G. V. Uitert, *J. Electrochem. Soc.*, 1967, **114**, 1048–1053.
38 P. Du, Y. Guo, S. H. Lee and J. S. Yu, *RSC Adv.*, 2017, **7**, 3170–3178.
39 J. Zheng, Q. Cheng, S. Wu, Z. Guo, Y. Zhuang, Y. Lu, Y. Li and C. Chen, *J. Mater. Chem. C*, 2015, **3**, 11219–11227.
40 E. Song, Y. Zhou, X.-B. Yang, Z. Liao, W. Zhao, T. Deng, L. Wang, Y. Ma, S. Ye and Q. Zhang, *ACS Photonics*, 2017, **4**, 2556–2565.
41 S. Bhushan and M. V. Chukichev, *J. Mater. Sci. Lett.*, 1988, **7**, 319–321.

